PHOTONICS Research

Ultrasensitive polarization-dependent terahertz modulation in hybrid perovskites plasmon-induced transparency devices

Junhu Zhou,[1,†] Yuze Hu,[1,†] Tian Jiang,[1,*,†] Hao Ouyang,[1] Han Li,[1] Yizhen Sui,[1] Hao Hao,[2] Jie You,[3] Xin Zheng,[3] Zhongjie Xu,[1] and Xiang'ai Cheng[1]

[1]College of Advanced Interdisciplinary Studies, National University of Defense Technology, Changsha 410073, China
[2]State Key Laboratory of High Performance Computing, College of Computer, National University of Defense Technology, Changsha 410073, China
[3]National Innovation Institute of Defense Technology, Academy of Military Sciences PLA China, Beijing 100071, China
*Corresponding author: tjiang@nudt.edu.cn

Received 26 April 2019; revised 12 June 2019; accepted 3 July 2019; posted 3 July 2019 (Doc. ID 366071); published 9 August 2019

Active control of metamaterial properties with high tunability of both resonant intensity and frequency is essential for advanced terahertz (THz) applications, ranging from spectroscopy and sensing to communications. Among varied metamaterials, plasmon-induced transparency (PIT) has enabled active control with giant sensitivity by embedding semiconducting materials. However, there is still a stringent challenge to achieve dynamic responses in both intensity and frequency modulation. Here, an anisotropic THz active metamaterial device with an ultrasensitive modulation feature is proposed and experimentally studied. A radiative-radiative-coupled PIT system is established, with a frequency shift of 0.26 THz in its sharp transparent windows by polarization rotation. Enabled by high charge-carrier mobility and longer diffusion lengths, we utilize a straightforwardly spin-coated $MAPbI_3$ film acting as a photoactive medium to endow the device with high sensitivity and ultrafast speed. When the device is pumped by an ultralow laser fluence, the PIT transmission windows at 0.86 and 1.12 THz demonstrate a significant reduction for two polarizations, respectively, with a full recovery time of 561 ps. In addition, we numerically prove the validity that the investigated resonator structure is sensitive to the optically induced conductivity. The hybrid system not only achieves resonant intensity and frequency modulations simultaneously, but also preserves the all-optical-induced switching merits with high sensitivity and speed, which enriches multifunctional subwavelength metamaterial devices at THz frequencies.

https://doi.org/10.1364/PRJ.7.000994

1. INTRODUCTION

Anisotropic optoelectronic devices have emerged as an attractive and appealing research subject due to the recent progress in photonics-based technologies, including communication, sensing, and molecular spectroscopy [1–4]. However, it is extremely hard to attain the intrinsic linear dichroism that is directly associated with the intrinsic nature of materials in the terahertz (THz) regime, which hinders the development of abundant anisotropic THz applications. Benefiting from the emergence of metamaterials, a variety of fascinating phenomena can be observed in their designed metal patterns, such as negative refraction [5], invisibility cloaking [6], hyperbolic media [7], perfect absorbers [8,9], chiral metamaterials [10], and superlenses [11], which are barely seen in natural materials. In this sense, it is possible to tailor the artificial metamaterials for accurate manipulation of THz-wave polarization and to exploit these materials with great flexibility.

To date, the integration of metamaterials with actively driven platforms by means of thermal [12,13], mechanical [14,15], optical [16–22], or electrical [23–25] control has triggered considerable interest, aiming at controlling and manipulating THz waves. More precisely, these approaches have successfully validated that the custom-built functionalities in the transmission of THz waves can be realized by either strength modulation or resonance frequency shifting. In the case of strength modulation, the near-field coupled metamaterials whose components are electromagnetically interfering with each other are more likely to be actively manipulated than the single metallic dipole resonators, mainly due to the enlarged influence induced by the disturbances of the interface environment. Recently, the Fano resonance-coupled optical-active THz metadevices for ultrasensitive and ultrafast photoactive switching have been realized, but with the drawback of single-frequency modulation [26]. When it comes to the

tuning of resonance frequency, active control of electromagnetically induced transparency has allowed a slight shifting of a Fano dip [27] frequency. A new device that is an electrically controlled connection between meta-atoms with graphene bridges has exhibited a dipole resonance shift up to 0.65 THz [28]. However, one significant disadvantage of such devices is their relatively low modulation speed driven by electricity, which may limit their application in ultrafast switching devices and modulating. From an alternative perspective, the polarization control may be viewed as a promising approach to adjust the resonance frequency without sacrificing the all-optical switching merits [29], such as sensitivity and high speed. The asymmetric Fano spectral profile and plasmon-induced transparency (PIT) phenomena are two prime examples of Fano resonance manifestation by mimicking quantum phenomena in classical metamaterial systems. In the case of PIT phenomenon, a sharp transparent window in the broad transmission dip is mainly contributed to by the destructive interference between two different modes. Following this definition, the PIT operating in the destructive interference between closed-ring resonators (CRRs) and split-ring resonators (SRRs) [30] could be engineered to generate an anisotropic Fano-type resonance. More precisely, this radiative-radiative coupling with a twofold symmetric structure can be endowed with sharp transparent windows at separate frequencies via polarization rotation.

As a dynamic medium, solution-processed $MAPbI_3$ films usually present an astonishing photon-photoconductivity ($\Delta\sigma$) conversion efficiency that determines the high sensitivity switching performance [31]. The use of organic-inorganic metal halide perovskite ($CH_3NH_3PbI_3$) has seen phenomenally rapid progress in the field of photovoltaic cells and photonic devices [32–36]. By virtue of high-charge carrier mobility ($\sim$500 $cm^2 \cdot V^{-1} \cdot s^{-1}$) [37–39], long diffusion length (beyond 1 μm), and high photoluminescence (PL) quantum yields (up to 90%) [40–45], perovskites have prompted intense research in power conversion efficiencies [46,47]. It is worth noting that the rapid recovery of charge carriers in perovskites has greatly facilitated high-speed optoelectronic devices beyond traditional silicon-based devices [48–50]. These outstanding properties laid the foundation for the design of photoactive media on resonant structures, with an extremely simple and economical spin-coating process. Herein, we demonstrate an ultrasensitive and high speed all-optical modulation of an anisotropic PIT resonator on the basis of an inexpensive, uncomplicated processing, and astonishing photoconductivity spin-coated $MAPbI_3$ perovskite film. The well optimized PIT resonance metaphotonic array demonstrates an outstanding dynamic response at the transmission windows of 0.86 and 1.12 THz for two perpendicular polarizations, respectively. The present work is an experimental demonstration of an anisotropic active THz metadevice fabricated in a simplified and cost-effective laboratory method.

2. RESULTS AND DISCUSSION

A. Sample Preparation and Characterization

The schematic architecture of the polarization-dependent metamaterial-perovskite THz device is presented in Fig. 1(a). A periodic array of SRRs and CRRs tailors the PIT resonance at different frequencies determined by incident THz polarizations. The detailed geometrical parameters are revealed in Fig. 1(b), which describes the metamaterial structure along with the unit cell dimensions. In this figure, two pairs of SRRs surround a CRR, with a bar located in the middle. Two aspectant SRRs aligned with CRR in the horizontal (x) direction (L_1, L_{21}, and L_{22}) have a different design compared to the other pair of SRRs in the vertical (y) direction (L_2, L_{12}, and L_{11}), which is the key point of the anisotropic PIT resonances. The metamaterial array is fabricated using the conventional photolithography technique, where the 127 nm thick gold (Au) structures is thermal-evaporated on a 2 mm thick z-cut quartz substrate as shown by the optical microscope image in Fig. 1(c). Au has excellent chemical stability and ultrahigh conductivity (over 4.56×10^7 S/m), which is often used as a perfect electrical conductor in THz structure arrays. The unit cell in the size of $P_x = 150$ μm, $P_y = 110$ μm is repeated in the x and y direction, respectively, eventually forming a rectangular array of 4 mm × 4 mm scale, as shown in Fig. 1(c).

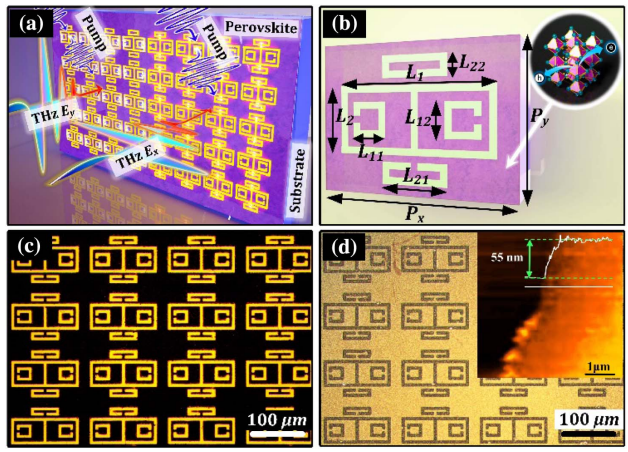

Fig. 1. (a) Schematic of the polarization-dependent metamaterial-perovskite THz device. A periodic array of CRRs and SRRs tailors the PIT resonance at different frequencies determined by incident polarizations. A thin perovskite film is deposited on the quartz substrate acting as a photoactive layer illuminated by optical pump pulses (400 nm). (b) Schematic view of the functional unit cell. The thickness of the quartz substrate is $H = 2$ mm, the height of the Au metamaterial is $h = 127$ nm, and the period is $P_x = 150$ μm, $P_y = 110$ μm. Geometric parameters of the structure are $L_1 = 120$ μm, $L_2 = 50$ μm, $L_{11} = 26$ μm, $L_{12} = 25$ μm, $L_{21} = 50$ μm, $L_{22} = 18$ μm, respectively. Inset presentation shows the crystal structure of T-$CH_3NH_3PbI_3$ phases. Optical microscopic images of fabricated Au structures (c) before and (d) after covering a 55 nm perovskite thin film, where the scale bar represents 100 μm, and the inset picture shows the thickness of the perovskite film.

With the metasurface ready, a 55 nm thin layer of solution process $MAPbI_3$ perovskite is spin-coated to obtain the hybrid metadevice [51–53]. In the hybrid metaphotonic device system, the properties of the photoactive medium are the dominant factors for the overall dynamical performance. A thin, dense, flat pinhole-free $MAPbI_3$ film is fabricated by spin-coating a perovskite precursor poly(ethylene oxide) (PEO) blend solution, followed by a thermal annealing process. Perovskite

precursor solution (10 wt%) is prepared by dissolving methylammonium iodide (MAI) and lead (II) iodide (PbI_2) powder with a 1:1 molar ratio in dimethyl sulfoxide (DMSO) at 70°C with vigorous stirring. PEO (3 wt% with respect to the $MAPbI_3$ precursor) is mixed with the precursor solution at 70°C. Before spin-coating, the prepared solution is cooled to room temperature and the metamaterial is cleaned by acetone, 2-propanol and UV–O_3 for 5 min each. Then the solution is spin-coated on the top of the metamaterial at 4000 r/min for 30 s in an N_2-filled glovebox. The as-spun device is immediately annealed by a hotplate at 85°C for 10 min, and the transparent film turned brown upon the evaporation of the DMSO. The metasurface is wholly covered and has a uniform surface morphology along with the structure array in Fig. 1(d). The high quality of perovskite film is verified by all the covered gaps between Au structures, which is especially important for near-field coupled resonances. An atomic force microscope (AFM) image inserted in Fig. 1(d) shows a clear stage of 55 nm thick film. In addition, we perform linear absorption and PL spectra tests on the prepared perovskite film. The film we used has a bandgap of 760 nm and an absorption peak at 740 nm (see Appendix A, Fig. 7).

B. Experimental Section

Optical characterization of the hybrid metamaterial-perovskite device is performed by the optical-pump-THz-probe (OPTP) method. Two 1 mm thick nonlinear crystals (ZnTe) are used in the THz generation and detection. The dynamic modulation process is recorded in the form of transient transmission amplitude change when the time delay of optical excitation pulse is step-changed from 0 to 600 ps. A Spectra Physics regenerative amplifier system, which can provide a 1 kHz pulse train of 800 nm (center wavelength) pulses of 100 fs duration (full width at half-maximum), is used as the light source of the whole OPTP setup. A part of 800 nm optical laser beam is frequency-doubled (400 nm) by 1 mm thick β-BaB_2O_4 crystal for optical pump of $MAPbI_3$ film, whose spot size is 5 mm in diameter, which is large enough to cover the THz beam spot (~2.2 mm in diameter) for a uniform excitation over the surface of the device. A wire-grid THz polarizer is used to project the polarization of THz pulses. The transmission spectra of the active device under different delay times and pump fluence $[E_S(\omega)]$ are normalized to the transmission spectra of reference substrate $[E_R(\omega)]$ following the relation of $|T(\omega)| = |E_S(\omega)/E_R(\omega)|$.

C. Simulation and Experiment Results

To investigate the polarization-dependent PIT properties of the designed structure, we numerically simulate and experimentally study the amplitude transmissions of the designed polarization-related metamaterial without perovskite coating, as shown in Fig. 2. To begin with, the numerical simulation results of the typical PIT windows at different frequencies for *x*-polarized and *y*-polarized incident waves are displayed in Fig. 2(a). In addition, the experimental data in Fig. 2(b) present that the PIT window is located at 0.81 THz for the *x*-polarized wave, while at 1.11 THz for the *y*-polarized wave, in good agreement with the simulated results of Fig. 2(a). As demonstrated in Fig. 1(a), the resonances of CRR and SRR are primarily

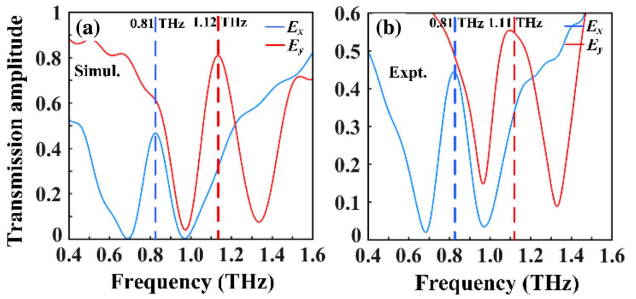

Fig. 2. (a) Simulated and (b) measured amplitude transmissions of the designed polarization-related metamaterial under illuminations of *x*-polarized (blue) and *y*-polarized (red) THz electric fields without perovskite coating. Dashed lines represent Fano-resonant frequencies for two polarized THz electric fields.

attributed to their geometrical dimensions via the THz illumination with a polarization along the gap. The strongly coupled electric dipole oscillation of CRR and the weakly coupled fundamental eigenmode of SRR excited by THz electric field are coupled back and forth through the magnetic field. Notably, the resonance frequency of SRR is slightly higher than the design compared to the dipole mode of CRR. In order to quantitatively determine the anisotropic functionality, our meta-atom sample consists of a CRR surrounded by two pairs of SRRs.

The CRR and its corresponding SRRs are designed with different sizes along the *x* and *y* axis, respectively. The displacement length in the middle of the CRRs and SRRs is set to be 5 μm to ensure enough coupling strength between each other. The strong coupling effect plays a key role in the giant enhancement of the THz electric field along the gap. Such coupling effects are demonstrated by the simulations of the intrinsic THz spectrum of CRR and SRR resonators [54] (see Appendix A, Fig. 8). In view of this, the enhanced mutual coupling between the SRR and CRR resonances exhibits unprecedented sensitivity of the gap environment, opening up new possibilities for ultrasensitive THz modulation beyond natural materials.

The strong resonance feature is still maintained in the experimentally measured transmission spectrum of the $MAPbI_3$ spin-coated sample. As presented in Figs. 3(a) and 3(c), the hybrid metaphotonic device holds a typical PIT resonance transmission spectrum that is similar to the result in Fig. 2(b) (*x* and *y* directions) when the pump beam is blocked, despite the influence imposed by the intrinsic conductivity of the perovskite film. In order to characterize such an influence on the PIT window, we take into account a series of the pump fluence of a 400 nm pulse, ranging from 5 to 240 μJ/cm^2. When the pump fluence is as low as 5 μJ/cm^2, as displayed in Figs. 3(a) and 3(c), the obvious modulation effect in the *x* direction and *y* direction can be clearly visualized in the transmission spectra. Specifically, the sharp PIT window is assigned to the destructive interference between the inductor-capacitor (LC) resonance and dipole resonance, which originate from the SRRs and CRRs, respectively. Once the 55 nm $MAPbI_3$ layer is excited by an increasing pump fluence, the screening effect of the fringing field by the $MAPbI_3$ layer is enhanced, while the PIT strength is gradually suppressed.

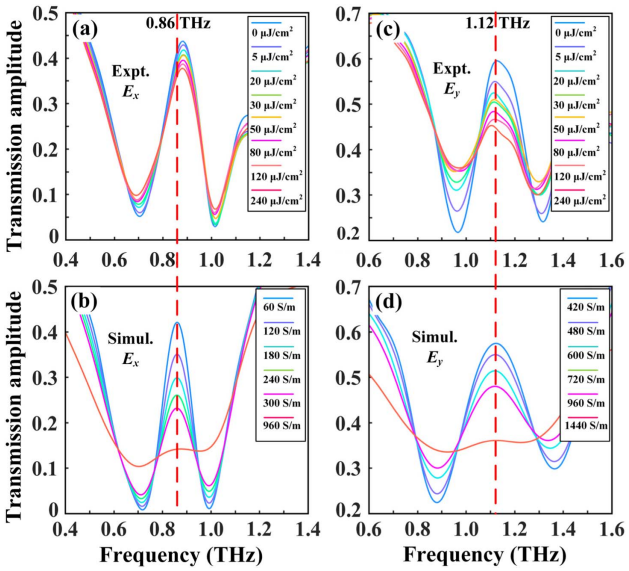

Fig. 3. Results of the optical modulation of anisotropic THz wave. Measured transmission spectra of the designed perovskite-based device of the (a) *x*-polarized and (c) *y*-polarized incident THz electric field under different pump powers. Corresponding numerically simulated transmission spectra of the (b) *x*-polarized and (d) *y*-polarized incident THz electric field under different conductivities of the perovskite thin film. The dashed lines mark the frequencies corresponding to the Fano resonance peaks.

In addition, the normalized ratio of transmission amplitude at the resonance peak of 0.86 and 1.12 THz along the *x* and *y* direction, respectively, is decreased from 0.44 and 0.60 to 0.37 and 0.45 when the pump fluence changes from 0 to 240 μJ/cm^2. This observed amplitude modulation of the PIT window is attributed to the reduced capacitance at the gap of CRRs and SRRs throughout the unit cell, which is the result of the optical excitation and photoconductivity of $MAPbI_3$ in the gap. In our study, the resonance peak (*y*) is not completely switched off, even though the modulation

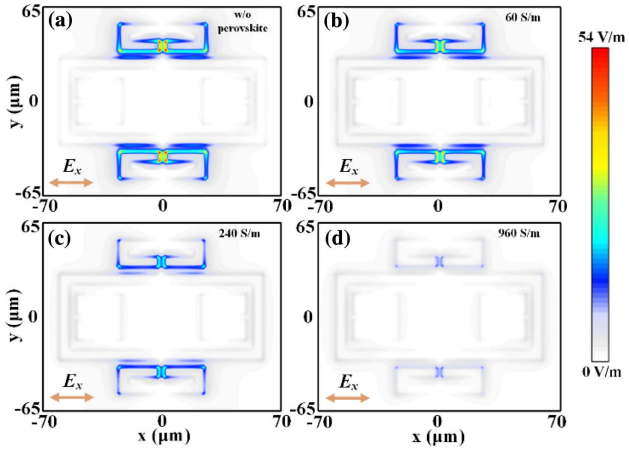

Fig. 4. Calculated *z*-component field distributions in the transverse plane of the Au metasurface varying the conductivity of the perovskite film under the *x*-polarized THz electric field from 0 S/m to 960 S/m. Incident fields are normalized as 1 V/m.

depth is already close to saturation under the pump fluence of 240 μJ/cm^2. From the simulation result [Fig. 3(d), 1440 S/m], the saturation of the modulation depth is actually derived from the photoconductivity response of the surface photoactive film. Considering that the photoactive film has a thickness of only 55 nm, this problem may be solved by appropriately increasing the thickness of the spin-coated perovskite. The anisotropic modulation is achieved under an ultralow pump fluence (5 μJ/cm^2), which is markedly different from previous studies [20,26,31] (detailed comparison is provided in Table 1). In fact, to improve the sensitivity of this device, we use perovskite as photoactive material and particularly employ a short gap (5 μm) design for the purpose of lowering the threshold to switch off the near-field coupling of LC resonance and dipole resonance. The effect of this design is certified by the simulation analysis shown in Figs. 3(b) and 3(d). The Lorentzian mechanical oscillator is a commonly used theoretical model for explaining the phenomenon of PIT metamaterial resonance [55,56]. We analyzed this PIT effect by theoretical calculation, as shown in Appendix A (Fig. 9). The modulation of the PIT peak can only be viewed as the change of the damping rate of SRR arms. Therefore, it indicates that the suppression of the bright mode in SRRs is the major factor of our modulation. Intending to rule out the fake PIT effect that may be hidden in the transmission amplitude [57], we extracted the group delay curves from the experimental results as the derivative of phase with respect to circular frequency. Significant slow-light effect is seen in Appendix A (Fig. 10), which could prove the authenticity of the PIT effect exhibited by our device.

From these figures, one can see that the resonance peaks almost disappear when the conductivity of the perovskite film is just set to a relatively low level, namely, 960 and 1440 S/m in the *x* and *y* direction, respectively. Importantly, this ultrasensitive (5 μJ/cm^2) resonant modulation behavior could open up a new direction for the design and construction of low-threshold perovskite-based plasmonic devices in the THz regime. Please note that the overall amplitude reduction in the excited ultrathin 55 nm thick perovskite can be negligible when compared to the modulation effect of the PIT resonance, since the electric field is tightly confined in the 5 μm gaps and enables an extremely sensitive response to the interface environment, resulting in the strong modulation of the PIT resonance. In addition, the experimental and simulation results exhibit a significant discrepancy in the modulation depth along the *x* polarization. Theoretical calculations show that the *x* direction is more sensitive than the *y* direction (the near-field simulation below gives an explanation), but experimentally, the modulation in the *x* direction is relatively small. This is due to the coupling effect of PIT resonance and optically active phonon mode of $MAPbI_3$ film, which was studied by earlier OPTP characterization at room temperature [26,58–60]. In the recent study [26], $MAPbI_3$ perovskite has shown an active phonon mode when the pump fluence is greater than 7 μJ/cm^2. The observed mode coupling of the phonon mode of the perovskite film with the dipole resonance (SRR resonator, Fig. 8 in Appendix A) at 1.0 THz in the former study could provide preliminary evidence for our experimental result (*x* direction,

Table 1. Some Reported Active Modulation of the Optically Controlled THz Modulator

Year	Active Material	Maximum Modulation Depth	Pump Wavelength and Minimum Working Fluence	Ref.
2018	310 nm Ge	29%	800 nm, 254 μJ/cm^2	[20]
2017	300 nm GaAs nanodisks	35%	800 nm, 310 μJ/cm^2	[61]
2017	400 nm, drop coated MoS_2 film	~20%	800 nm, 12.7 μJ/cm^2	[18]
2012	500 nm Si	49%	800 nm, 35 μJ/cm^2	[50]
2018	284 nm VO_2 film	138 deg (phase shifting)	800 nm (cw laser), 3.5 W/cm^2	[13]
2018	50 nm high-T_c YBCO	42%	800 nm, 64 μJ/cm^2	[62]
This work	55 nm $MAPbI_3$ film	25%	400 nm, 5 μJ/cm^2	This work

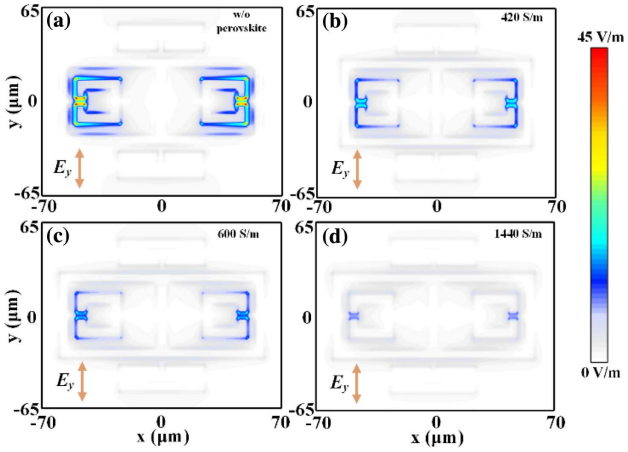

Fig. 5. Calculated z-component field distributions in the transverse plane of the Au metasurface varying the conductivity of the perovskite film under the y-polarized THz electric field from 0 S/m to 1440 S/m. Incident fields are normalized as 1 V/m.

at ~0.86 THz), which is repeatedly tested. In order to more intuitively reflect the influence of the coupling between the phonon mode and the PIT resonance mode on the device, we verified it by the simulation with the addition of the phonon mode (see Appendix A, Fig. 11).

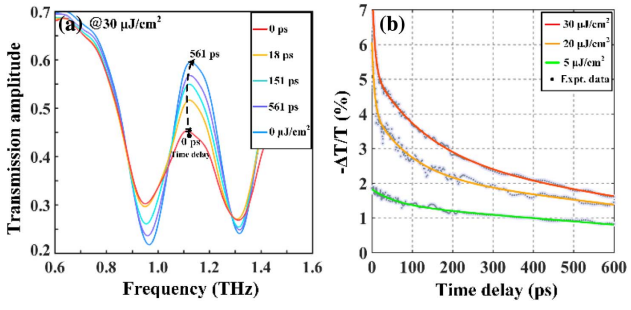

Fig. 6. Time-evolution dynamics of the metasurface-perovskite device. (a) Transient transmission spectra of the y-polarized THz electric field at different pump-probe delay values for an average pump fluence of 30 μJ/cm^2. (b) Measured transient THz excitation dynamics for perovskite ($CH_3NH_3PbI_3$) thin film spin-coated on the Fano-resonant metasurface implemented by using OPTP measurements for various pump fluences. Solid curves represent the fittings of recombination processes utilizing rate equations, where the dotted lines are measured by experiment.

To clarify the underlying mechanism of the modulation effect in Fig. 3, a commonly used finite-element method is employed to analyze the electric field distributions, considering various conductivities of the perovskite film. As described in Fig. 1(b), a base unit cell is illuminated by the incident THz radiation with an electric field intensity of 1 V/m. Here, the Floquet boundary condition is utilized to describe the continuous metamaterial arrays. In consideration that the influence of resonance is best exemplified by the z component of electric field E_z, which is located 27.5 nm above the upper surface of the substrate, it is shown to characterize resonant behaviors at the center of PIT windows. Since the aforementioned resultant transmission through the perovskite-based anisotropic THz device is a function of frequency, PIT peaks exist at 0.86 and 1.12 THz for x- and y-polarized THz incidences, respectively. Therefore, we restrict our attention to the electric fields with various perovskite film conductivities at both of these frequencies, in order to investigate the change of electric field concentrated at the gaps of the metamaterial structure.

One significant finding from Fig. 4(a) is that the electric field confinement in the gap along the x-polarized THz wave is around 54 times stronger than in the other region, allowing for a giant sensitivity of conductivity change within the gap along the x axis. Particularly, the electric field in the CRR is almost completely suppressed, which identifies and characterizes the feature of a typical PIT effect. Without an optical pump, the perovskite thin film can be considered as a semiconductor with small conductivity of 60 S/m, and the resonators exhibit very strong electric confinement, which is comparable to the case without perovskite, as presented in Fig. 4(b). On photoexcitation, the controllably increased conductivity induced by the pump beam allows for the active tuning under variable coupling strengths with specified polarization direction. It is visible that the electric field enhancement shows a moderate and even strong attenuation when the perovskite conductivity goes up to 240 S/m and 960 S/m, respectively. This confirms the weakening coupling between CRR and SRR, as we predicted in previous sections. The underlying physics can be intuitively understood as follows: the radiative LC mode resonance in the SRR pair is hampered by the photoexcitation enhancement, leading to a weaker circulating current in the SRR pair. Based on this mechanism, we reiterate the designed structure as the image illustrated in Fig. 1 to provide a deeper insight into this process. Two gaps, namely, the gap between the CRR and SRR and the gap in the SRR, would be connected by the perovskite film with a considerably high conductivity. Hence, the circulating current of SRR is difficult to be

generated by strong oscillation with the incident THz wave. On the other hand, the electric field confinement of 1.12 THz in the gap along the y-axis direction corresponding to the y-polarized THz incidence shows similar patterns with the change of optically controlled conductivity, as illustrated in Fig. 5. These results contribute to the effective and active modulations of meta-atoms via optical control of the perovskite conductance.

In order to explore the dynamic response of ultrafast modulation aspect, we have experimentally characterized the temporary resonant switching behavior in our proposed perovskite-functionalized metamaterial hybrid device. For illustration, the temporal evolution of the dynamic modulation response in y polarization and the transient transmission amplitude change of solution spin-coated perovskite film on quartz in the absence of Au structure are shown in Fig. 6. Notably, the relative time delay between the pump and the THz probe is controlled by a step motor, and the 400 nm pump pulse is assumed to stimulate the sample at a 0 ps time delay. A main conclusion from Fig. 6(a) is that under a 30 $\mu J/cm^2$ pump fluence, the PIT amplitude at the frequency of 1.12 THz gradually restores from the state at 0 ps time delay and becomes very close to the original transmission amplitude without photoexcitation at 561 ps. It can be seen that our sample exhibits a faster response speed (<1 ns, GHz) than the millisecond response of conventional silicon-based photoactive devices. The heavily curtailed PIT amplitude at a 0 ps time delay implies that the maximum density of photoexcited carriers exists in the perovskite film.

In Fig. 6(a), we use the transmission amplitude of the PIT resonance

$$\frac{E_t - E_{\text{on}}}{E_{\text{off}} - E_{\text{on}}} \times 100\%, \tag{1}$$

to quantify the recovery of device. E_{off} is the PIT amplitude without pump, E_{on} is the PIT amplitude at the time delay of 0 ps, and E_t is the PIT amplitude at the time delay of t. Among the time delays of 18, 151, and 561 ps, the calculation results of recovery ratio are 43.3%, 66.7%, and 82.3%, respectively. And the recovery rate of the PIT response is progressively decreased, as revealed in the recombination curve of the nonequilibrium carriers from Fig. 6(b). By step-collecting the change of amplitude (ΔT) throughout the delay line at the peak THz transient signal (T), time-resolved relaxing of photoconductivity in the $MAPbI_3$ film is obtained as $-\Delta T/T$, which is proportional to $\Delta\sigma$. Unlike the PIT resonance, which is more susceptible to interface environment, the light-induced change of perovskite film is relatively small (where the maximum is ~7% under a 30 $\mu J/cm^2$ pump fluence) and displays a clear pump power dependence. Extracting the characteristic time from this temporal evolution is essential for the study of other $MAPbI_3$-based devices. At the pump fluence of 20 and 30 $\mu J/cm^2$, a triple-exponential decay equation,

$$-\frac{\Delta T}{T}(t) = A_1 e^{-\frac{t}{t_1}} + A_2 e^{-\frac{t}{t_2}} + A_3 e^{-\frac{t}{t_3}} + A_0, \tag{2}$$

is used to fit the dynamic curves for the presence of trimolecular processes (Auger recombination). Meanwhile, at the lowest fluence, a double-exponential expression,

$$-\frac{\Delta T}{T}(t) = A_1 e^{-\frac{t}{t_1}} + A_2 e^{-\frac{t}{t_2}} + A_0, \tag{3}$$

is more suitable for the bimolecular recombination-dominated process. Because the first-order recombination process (i.e., the trap-assisted monomolecular recombination) is reported to last longer than 10 ns, far beyond the delay line in the $MAPbI_3$ sample, we fix the decay time constant t_1 at 10 ns for convenience [41]. The best-fitting curves are shown as solid lines in Fig. 6(b). Additionally, the trimolecular decay time constant t_3 at 20 and 30 $\mu J/cm^2$ is obtained to be 6.2 and 6.7 ps, respectively. What follows is the bimolecular decay time constant t_2, which is 63, 96, and 141 ps for the 5, 20, and 30 $\mu J/cm^2$ pump fluence, respectively. This indicates that the fast decay process (i.e., the second- and third-order recombination) of photoconductivity in perovskite film is mainly completed within ~200 ps, which is consistent with the result of Fig. 6(a), where the response of PIT resonance is quickly repaired within 151 ps and then changed slowly. It is well known that the trap-assisted monomolecular recombination rate of the $MAPbI_3$ perovskite is exceptionally low, and the carriers' relaxation curve can be high-quality fitted when just incorporating bimolecular and trimolecular decay components [48]. Based on this point—that the first-order decay can be ignored—we can understand the weak effect of a slow recombination process on device response speed. Therefore, it can be concluded that the high-speed response of our sample is caused by the fast recombination process (i.e., the second- and third-order recombination) of nonequilibrium carriers.

3. CONCLUSION

In summary, we have experimentally demonstrated the ultrasensitive modulation (5 $\mu J/cm^2$) and THz transmission modulation characteristics of an active metamaterial device by constructing a perovskite-hybridized anisotropic PIT resonator array with a spin-coated 55 nm $MAPbI_3$ film as the photoactive medium. The high-speed dynamic behavior of all-optical modulation along the x and y polarizations with different PIT frequencies is obtained with a giant sensitivity and a far faster speed compared to silicon-based devices, which implies the excellent potential of easily solution-processed perovskite in application of fast optical response devices. Moreover, we have performed accurate numerical simulations that prove that our resonator structure is sensitive to the surface dielectric environment, a prerequisite for weak-light detection and sensing. Further, the polarization-dependent design has provided a promising alternative to modulate the resonance frequency while preserving the all-optical switching merits (e.g., high sensitivity and ultrafast speed). Therefore, the anisotropic PIT structure can be regarded as a potential candidate for multifunctional subwavelength metamaterial devices operating in the THz range.

APPENDIX A

The physical origin of photon-active modulation of the near-field coupling effect between two bright models in the hybrid perovskites metasurface is explained by a typical coupled harmonic oscillator model.

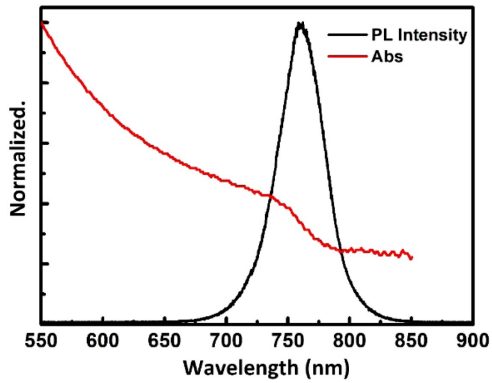

Fig. 7. Normalized linear absorption and PL spectra of the spin-coated perovskite ($CH_3NH_3PbI_3$) film. The PL and absorption peaks are located at 760 and 740 nm, respectively.

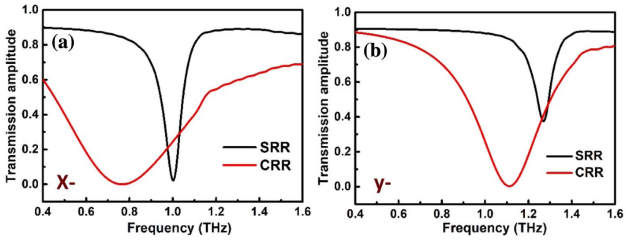

Fig. 8. Intrinsic THz spectra of SRR and CRR resonators along (a) x and (b) y directions. The near-field coupling effect between CRR and SRR is the origin of PIT resonance.

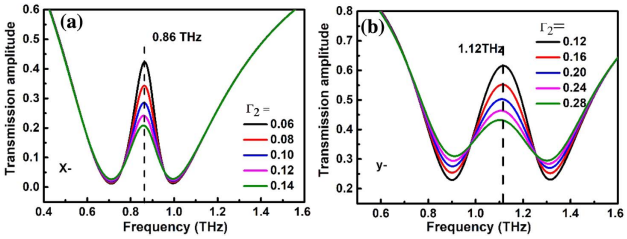

Fig. 9. Theoretical calculation results of the Lorentzian mechanical oscillator model along the (a) x-polarized and (b) y-polarized incident THz electric field.

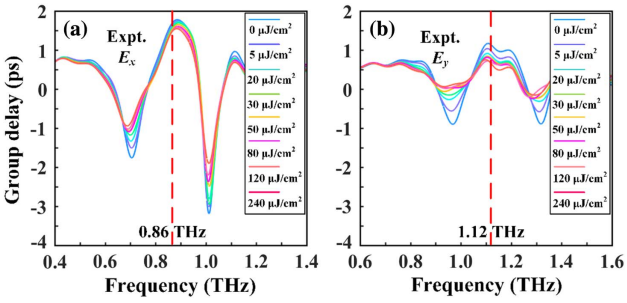

Fig. 10. Group delay data extracted from experiment results as a function of pump fluence: (a) x-direction and (b) y-direction.

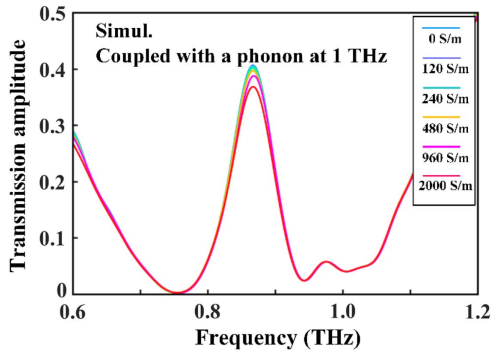

Fig. 11. Simulated results with a phonon mode at 1.0 THz in the perovskite thin film as a function of optical conductivity of the perovskite thin film.

$$\omega_1^{-2}\ddot{p}(t) + \Gamma_1\omega_1^{-1}\dot{p}(t) + p(t) = f(t) - \kappa q(t),$$
$$\omega_2^{-2}\ddot{q}(t) + \Gamma_2\omega_2^{-1}\dot{q}(t) + q(t) = -\kappa p(t), \quad \textbf{(A1)}$$

where κ is the linear coupling strength between the two resonators. Γ_1, Γ_2, ω_1, and ω_2 are damping factors and resonance frequencies of the two bright (CRR and SRR) resonators. Γ_1 and Γ_2 are defined by the excitation $p(t)$ and $q(t)$, respectively. $f(t)$ is the external motivating force that projects Γ_2. We could express the susceptibility $\tilde{\chi}_e$ as a function of the above-mentioned parameters, and then the transmission amplitude can be calculated from the susceptibility [56].

In order to explain the relative lower modulation depth along the x polarization, a Lorentz–Drude model is used here to determine the material properties as

$$\sigma(\omega) = -i\varepsilon_0\omega(\varepsilon_\infty - 1) + \sum_{m=1}\frac{\varepsilon_0\omega_{p,m}^2\omega}{i(\omega_{0,m}^2 - \omega^2) + \omega\Gamma_m} + i\frac{\sigma}{\omega\varepsilon_0}, \quad \textbf{(A2)}$$

where $\omega_{p,m}$, $\omega_{0,m}$, and Γ_m are plasma frequencies, phonon resonance frequencies, and the scattering rate, respectively. σ is the optical conductivity generated by the optical pump. We utilized this model to roughly describe the coupled phonon mode and optical conductivity of perovskite film.

A wide array of photosensitive materials is explored for the advancement of active THz metadevices, including semiconductors (Ge, GaAs, Si, and perovskites), 2D transition metal dichalcogenides (MoS_2), phase-change materials (VO_2), and superconductors (YBCO). Traditional semiconductors such as Ge, Si, and GaAs generally have a large thickness (~300 nm) when used as a photon doping medium, and their pump fluence usually needs more than 100 $\mu J/cm^2$. There are few reports on the use of chemical vapor deposition (CVD)-grown large-area transition metal dichalcogenides (TMDCs) film for THz metasurfaces, but the application of MoS_2 nanosheets on the surface of metal structures has achieved a good all-optical modulation effect. The optical properties of superconductors and phase change materials are usually related to the ambient temperature, and a high power is required when their state is significantly changed by means of optical pumping. In this work, our device can work at pump fluence as low as 5 $\mu J/cm^2$, and this result is based on the premise that our

perovskite thin film is only 55 nm thick. If the thickness of the film is appropriately increased, the modulation depth of our device may be better.

Funding. National Natural Science Foundation of China (NSFC) (11802339, 11804387, 11805276, 61801498, 61805282); Scientific Researches Foundation of National University of Defense Technology (ZK16-03-59, ZK18-01-03, ZK18-03-22, ZK18-03-36); Natural Science Foundation of Hunan Province (2016JJ1021); Open Director Fund of State Key Laboratory of Pulsed Power Laser Technology (SKL2018ZR05); Open Research Fund of Hunan Provincial Key Laboratory of High Energy Technology (GNJGJS03); Opening Foundation of State Key Laboratory of Laser Interaction with Matter (SKLLIM1702); Youth Talent Lifting Project (17-JCJQ-QT-004).

†These authors contributed equally to this work.

REFERENCES

1. G. P. Neupane, K. Zhou, S. Chen, T. Yildirim, P. Zhang, and Y. Lu, "In-plane isotropic/anisotropic 2D van der Waals heterostructures for future devices," Small **15**, 1804733 (2019).
2. W. Zhou, J. Chen, H. Gao, T. Hu, S. Ruan, A. Stroppa, and W. Ren, "Anomalous and polarization-sensitive photo-response of Td-WTe_2 from visible to infrared light," Adv. Mater. **31**, 1804629 (2018).
3. J. Liu, Y. Zhou, Y. Lin, M. Li, H. Cai, Y. Liang, M. Liu, Z. Huang, F. Lai, F. Huang, and W. Zheng, "Anisotropic photo-response of the ultrathin GeSe nanoplates grown by rapid physical vapor deposition," ACS Appl. Mater. Interfaces **11**, 4123–4130 (2019).
4. Z. Zhou, M. Long, L. Pan, X. Wang, M. Zhong, M. Blei, J. Wang, J. Fang, S. Tongay, W. Hu, J. Li, and Z. Wei, "Perpendicular optical reversal of the linear dichroism and polarized photodetection in 2D GeAs," ACS Nano **12**, 12416–12423 (2018).
5. S. Yoo, S. Lee, and Q.-H. Park, "Loss-free negative-index metamaterials using forward light scattering in dielectric meta-atoms," ACS Photon. **5**, 1370–1374 (2018).
6. R. Schittny, M. Kadic, T. Buckmann, and M. Wegener, "Invisibility cloaking in a diffusive light scattering medium," Science **345**, 427–429 (2014).
7. R. Macedo, T. Dumelow, R. E. Camley, and R. L. Stamps, "Oriented asymmetric wave propagation and refraction bending in hyperbolic media," ACS Photon. **5**, 5086–5094 (2018).
8. Y. S. Jonathan, F. Kebin, and J. P. A. Willie, "Zero-rank, maximum nullity perfect electromagnetic wave absorber," Adv. Opt. Mater. **7**, 1801632 (2019).
9. X. Zhao, Y. Wang, J. Schalch, G. Duan, K. Cremin, J. Zhang, C. Chen, D. R. Averitt, and X. Zhang, "Optically modulated ultra-broadband all-silicon metamaterial terahertz absorbers," ACS Photon. **6**, 830–837 (2019).
10. Z. Wang, B. Ai, Z. Zhou, Y. Guan, H. Möhwald, and G. Zhang, "Free-standing plasmonic chiral metamaterials with 3D resonance cavities," ACS Nano **12**, 10914–10923 (2018).
11. Q. Yang, J. Gu, Y. Xu, X. Zhang, Y. Li, C. Ouyang, Z. Tian, J. Han, and W. Zhang, "Broadband and robust metalens with nonlinear phase profiles for efficient terahertz wave control," Adv. Opt. Mater. **5**, 1601084 (2017).
12. M. T. Nouman, J. Hwang, M. Faiyaz, G. Lee, D. Y. Noh, and J.-H. Jang, "Dynamic metasurface based cavity structures for enhanced absorption and phase modulation," ACS Photon. **6**, 374–381 (2019).
13. Y. Zhao, Y. Zhang, Q. Shi, S. Liang, W. Huang, W. Kou, and Z. Yang, "Dynamic photoinduced controlling of the large phase shift of terahertz waves via vanadium dioxide coupling nanostructures," ACS Photon. **5**, 3040–3050 (2018).
14. M. Manjappa, P. Pitchappa, N. Wang, C. Lee, and R. Singh, "Active control of resonant cloaking in a terahertz MEMS metamaterial," Adv. Opt. Mater. **6**, 1800141 (2018).
15. L. Cheng, Z. Jin, Z. Ma, F. Su, Y. Zhao, Y. Zhang, T. Su, Y. Sun, X. Xu, Z. Meng, Y. Bian, and Z. Sheng, "Mechanical terahertz modulation based on single-layered graphene," Adv. Opt. Mater. **6**, 1700877 (2018).
16. P. Pitchappa, A. Kumar, S. Prakash, H. Jani, T. Venkatesan, and R. Singh, "Chalcogenide phase change material for active terahertz photonics," Adv. Mater. **31**, 1808157 (2019).
17. H. Cai, Q. Huang, X. Hu, Y. Liu, Z. Fu, Y. Zhao, H. He, and Y. Lu, "All-optical and ultrafast tuning of terahertz plasmonic metasurfaces," Adv. Opt. Mater. **6**, 1800143 (2018).
18. Y. K. Srivastava, A. Chaturvedi, M. Manjappa, A. Kumar, G. Dayal, C. Kloc, and R. Singh, "MoS_2 for ultrafast all-optical switching and modulation of THz Fano metaphotonic devices," Adv. Opt. Mater. **5**, 1700762 (2017).
19. A. Kumar, Y. K. Srivastava, M. Manjappa, and R. Singh, "Color-sensitive ultrafast optical modulation and switching of terahertz plasmonic devices," Adv. Opt. Mater. **6**, 1800030 (2018).
20. W. X. Lim, M. Manjappa, Y. K. Srivastava, L. Cong, A. Kumar, K. F. MacDonald, and R. Singh, "Ultrafast all-optical switching of germanium-based flexible metaphotonic devices," Adv. Mater. **30**, 1705331 (2018).
21. J. Gu, R. Singh, X. Liu, X. Zhang, Y. Ma, S. Zhang, A. S. Maier, Z. Tian, K. Azad, A. Chen, H.-T. Chen, A. Taylor, J. Han, and W. Zhang, "Active control of electromagnetically induced transparency analogue in terahertz metamaterials," Nat. Commun. **3**, 1151 (2012).
22. L. Cong, Y. K. Srivastava, H. Zhang, X. Zhang, J. Han, and S. Ranjan, "All-optical active THz metasurfaces for ultrafast polarization switching and dynamic beam splitting," Light Sci. Appl. **7**, 28 (2018).
23. H. Jung, H. Jo, W. Lee, B. Kim, H. Choi, M. S. Kang, and H. Lee, "Electrical control of electromagnetically induced transparency by terahertz metamaterial funneling," Adv. Opt. Mater. **7**, 1801205 (2018).
24. Z. Chen, X. Chen, L. Tao, K. Chen, M. Long, X. Liu, K. Yan, R. I. Stantchev, E. Pickwell-MacPherson, and J.-B. Xu, "Graphene controlled Brewster angle device for ultra-broadband terahertz modulation," Nat. Commun. **9**, 4909 (2018).
25. T.-T. Kim, H.-D. Kim, R. Zhao, S. S. Oh, T. Ha, D. S. Chung, Y. H. Lee, B. Min, and S. Zhang, "Electrically tunable slow light using graphene metamaterials," ACS Photon. **5**, 1800–1807 (2018).
26. M. Manjappa, Y. K. Srivastava, A. Solanki, A. Kumar, T. C. Sum, and R. Singh, "Hybrid lead halide perovskites for ultrasensitive photoactive switching in terahertz metamaterial devices," Adv. Mater. **29**, 1605881 (2017).
27. S. J. Kindness, N. W. Almond, B. Wei, R. Wallis, W. Michailow, V. S. Kamboj, P. Braeuniger-Weimer, S. Hofmann, H. E. Beere, D. A. Ritchie, and R. Degl'Innocenti, "Active control of electromagnetically induced transparency in a terahertz metamaterial array with graphene for continuous resonance frequency tuning," Adv. Opt. Mater. **6**, 1800570 (2018).
28. H. Jung, J. Koo, E. Heo, B. Cho, C. In, W. Lee, H. Jo, J. H. Cho, H. Choi, M. S. Kang, and H. Lee, "Electrically controllable molecularization of terahertz meta-atoms," Adv. Mater. **30**, 1802760 (2018).
29. X. Chen, S. Ghosh, Q. Xu, C. Ouyang, Y. Li, X. Zhang, Z. Tian, J. Gu, L. Liu, A. K. Azad, J. Han, and W. Zhang, "Active control of polarization-dependent near-field coupling in hybrid metasurfaces," Appl. Phys. Lett. **113**, 061111 (2018).
30. M. Liu, Z. Tian, X. Zhang, J. Gu, C. Ouyang, J. Han, and W. Zhang, "Tailoring the plasmon-induced transparency resonances in terahertz metamaterials," Opt. Express **25**, 19844–19855 (2017).
31. L. Q. Cong, K. S. Yogesh, S. Ankur, C. S. Tze, and S. Ranjan, "Perovskite as a platform for active flexible metaphotonic devices," ACS Photon. **4**, 1595–1601 (2017).
32. T. W. Crothers, R. L. Milot, J. B. Patel, E. S. Parrott, J. Schlipf, P. Müller-Buschbaum, M. B. Johnston, and L. M. Herz, "Photon reabsorption masks intrinsic bimolecular charge-carrier recombination in $CH_3NH_3PbI_3$ perovskite," Nano Lett. **17**, 5782–5789 (2017).

33. S.-F. Leung, K.-T. Ho, P.-K. Kung, V. K. S. Hsiao, H. N. Alshareef, Z. L. Wang, and J.-H. He, "A self-powered and flexible organometallic halide perovskite photodetector with very high detectivity," Adv. Mater. **30**, 1704611 (2018).
34. L. Najafi, B. Taheri, B. Martín-García, S. Bellani, D. D. Girolamo, A. Agresti, R. Oropesa-Nunez, S. Pescetelli, L. Vesce, E. Calabro, M. Prato, A. E. D. R. Castillo, A. D. Carlo, and F. Bonaccorso, "MoS_2 quantum dot/graphene hybrids for advanced interface engineering of a $CH_3NH_3PbI_3$ perovskite solar cell with an efficiency of over 20%," ACS Nano **12**, 10736–10754 (2018).
35. J. Zhen, W. Zhou, M. Chen, B. Li, L. Jia, M. Wang, and S. Yang, "Pyridine-functionalized fullerene additive enabling coordination interactions with $CH_3NH_3PbI_3$ perovskite towards highly efficient bulk heterojunction solar cells," J. Mater. Chem. A **7**, 2754–2763 (2019).
36. M. H. Laura, "Charge-carrier dynamics in organic-inorganic metal halide perovskites," Annu. Rev. Phys. Chem. **67**, 65–89 (2016).
37. D. A. Valverde-Chávez, C. S. Ponseca, C. C. Stoumpos, A. Yartsev, M. G. Kanatzidis, V. Sundström, and D. G. Cooke, "Intrinsic femtosecond charge generation dynamics in single crystal $CH_3NH_3PbI_3$," Energy Environ. Sci. **8**, 3700–3707 (2015).
38. Q. Dong, Y. Fang, Y. Shao, P. Mulligan, J. Qiu, L. Cao, and J. Huang, "Electron-hole diffusion lengths > 175 μm in solution-grown $CH_3NH_3PbI_3$ single crystals," Science **347**, 967–970 (2015).
39. O. E. Semonin, G. A. Elbaz, D. B. Straus, T. D. Hull, D. W. Paley, A. M. van der Zande, J. C. Hone, I. Kymissis, C. R. Kagan, X. Roy, and J. S. Owen, "Limits of carrier diffusion in n-type and p-type $CH_3NH_3PbI_3$ perovskite single crystals," J. Phys. Chem. Lett. **7**, 3510–3518 (2016).
40. Y. Kim, E. Yassitepe, O. Voznyy, R. Comin, G. Walters, X. Gong, P. Kanjanaboos, A. F. Nogueira, and E. H. Sargent, "Efficient luminescence from perovskite quantum dot solids," ACS Appl. Mater. Interfaces **7**, 25007–25013 (2015).
41. F. Zhang, H. Zhong, C. Chen, X.-G. Wu, X. Hu, H. Huang, J. Han, B. Zou, and Y. Dong, "Brightly luminescent and color-tunable colloidal $CH_3NH_3PbX_3$ (X = Br, I, Cl) quantum dots: potential alternatives for display technology," ACS Nano **9**, 4533–4542 (2015).
42. Q. A. Akkerman, V. D'Innocenzo, S. Accornero, A. Scarpellini, A. Petrozza, M. Prato, and L. Manna, "Tuning the optical properties of cesium lead halide perovskite nanocrystals by anion exchange reactions," J. Am. Chem. Soc. **137**, 10276–10281 (2015).
43. K. Wei, T. Jiang, Z. Xu, J. Zhou, J. You, Y. Tang, H. Li, R. Chen, X. Zheng, S. Wang, K. Yin, Z. Wang, J. Wang, and X. Cheng, "Ultrafast carrier transfer promoted by interlayer Coulomb coupling in 2D/3D perovskite heterostructures," Laser Photon. Rev. **12**, 1800128 (2018).
44. H. Li, X. Zheng, Y. Liu, Z. P. Zhang, and T. Jiang, "Ultrafast interfacial energy transfer and interlayer excitons in the monolayer WS_2/$CsPbBr_3$ quantum dot heterostructure," Nanoscale **10**, 1650–1659 (2018).
45. K. Wei, Z. J. Xu, R. Z. Chen, X. Zheng, X. A. Cheng, and T. Jiang, "Temperature-dependent excitonic photoluminescence excited by two-photon absorption in perovskite $CsPbBr_3$ quantum dots," Opt. Lett. **41**, 3821–3824 (2016).
46. X. Guichuan, M. Nripan, S. L. Swee, Y. Natalia, L. Xinfeng, S. Dharani, G. Michael, M. Subodh, and C. S. Tze, "Low-temperature solution-processed wavelength-tunable perovskites for lasing," Nat. Mater. **13**, 476–480 (2014).
47. J. H. Heo, S. H. Im, J. H. Noh, T. N. Mandal, C. S. Lim, J. A. Chang, Y. H. Lee, H.-J. Kim, A. Sarkar, M. K. Nazeeruddin, M. Grätzel, and S. Seok, "Efficient inorganic-organic hybrid heterojunction solar cells containing perovskite compound and polymeric hole conductors," Nat. Photonics **7**, 486–491 (2013).
48. W. Christian, E. E. Giles, B. J. Michael, J. S. Henry, and M. H. Laura, "High charge carrier mobilities and lifetimes in organolead trihalide perovskites," Energy Environ. Sci. **7**, 2269 (2014).
49. W. S. De, J. Holovsky, S. J. Moon, P. L. Per, B. Niesen, M. Ledinsky, F. J. Haug, J.-H. Yum, and C. Ballif, "Organometallic halide perovskites: sharp optical absorption edge and its relation to photovoltaic performance," J. Phys. Chem. Lett. **5**, 1035–1039 (2014).
50. J. Gu, R. Singh, X. Liu, X. Zhang, Y. Ma, S. Zhang, A. S. Maier, Z. Tian, K. Azad, A. Chen, H.-T. Chen, A. Taylor, J. Han, and W. Zhang, "Active control of electromagnetically induced transparency analogue in terahertz metamaterials," Nat. Commun. **3**, 1151 (2012).
51. H. Cho, S.-H. Jeong, M.-H. Park, Y.-H. Kim, C. Wolf, C.-L. Lee, J. H. Heo, A. Sadhanala, N. Myoung, S. Yoo, S. H. Im, R. H. Friend, and T.-W. Lee, "Overcoming the electroluminescence efficiency limitations of perovskite light-emitting diodes," Science **350**, 1222–1225 (2015).
52. M. M. Lee, J. Teuscher, T. Miyasaka, T. N. Murakami, and H. J. Snaith, "Efficient hybrid solar cells based on meso-superstructured organometal halide perovskites," Science **338**, 643–647 (2012).
53. B. Jeong, H. Han, Y. J. Choi, S. H. Cho, E. H. Kim, S. W. Lee, J. S. Kim, C. Park, D. Kim, and C. Park, "All-inorganic $CsPbI_3$ perovskite phase-stabilized by poly(ethylene oxide) for red-light-emitting diodes," Adv. Funct. Mater. **28**, 1706401 (2018).
54. C. W. Singh, R. Zhang, C. J. G. Han, M. Tonouchi, and W. L. Zhang, "Plasmon-induced transparency in metamaterials: active near field coupling between bright superconducting and dark metallic mode resonators," Appl. Phys. Lett. **103**, 101106 (2013).
55. X. Zhang, N. Xu, K. Qu, Z. Tian, R. Singh, J. Han, and W. L. Zhang, "Electromagnetically induced absorption in a three-resonator metasurface system," Sci. Rep. **5**, 10737 (2015).
56. P. Tassin, L. Zhang, R. Zhao, A. Jain, T. Koschny, and C. M. Soukoulis, "Electromagnetically induced transparency and absorption in metamaterials: the radiating two-oscillator model and its experimental confirmation," Phys. Rev. Lett. **109**, 187401 (2012).
57. A. S. Roberts, D. Wang, D. Fei, D. Wang, P. K. Kristensen, S. I. Bozhevolnyi, and K. Pedersen, "Multilayer tungsten-alumina-based broadband light absorbers for high-temperature applications," Opt. Mater. Express **6**, 2704–2714 (2016).
58. C. Laovorakiat, J. M. Kadro, T. Salim, D. Zhao, T. Ahmed, Y. M. Lam, J. X. Zhu, R. A. Marcus, M. E. Michel-Beyerle, and E. E. M. Chia, "Phonon mode transformation across the orthohombic-tetragonal phase transition in a lead-iodide perovskite $CH_3NH_3PbI_3$: a terahertz time-domain spectroscopy approach," J. Phys. Chem. Lett. **7**, 1–6 (2016).
59. M. Bokdam, T. Sander, A. Stroppa, S. Picozzi, D. D. Sarma, C. Franchini, and G. Kresse, "Role of polar phonons in the photo excited state of metal halide perovskites," Sci. Rep. **6**, 28618 (2016).
60. C. La-o-vorakiat, L. Cheng, T. Salim, R. A. Marcus, M. E. M. Beyerle, Y. M. Lam, and E. E. M. Chia, "Hybrid tandem quantum dot/organic photovoltaic cells with complementary near infrared absorption," Appl. Phys. Lett. **110**, 123901 (2017).
61. M. R. Shcherbakov, S. Liu, V. V. Zubyuk, A. Vaskin, P. P. Vabishchevich, G. Keeler, T. Pertsch, T. V. Dolgova, I. Staude, I. Brener, and A. A. Fedyanin, "Ultrafast all-optical tuning of direct-gap semiconductor metasurfaces," Nat. Commun. **8**, 17 (2017).
62. Y. K. Srivastava, M. Manjappa, L. Cong, H. N. S. Krishnamoorthy, V. Savinov, P. Pitchappa, and R. Singh, "A superconducting dual-channel photonic switch," Adv. Mater. **30**, 1801257 (2018).